ADVANCED ENERGY MATERIALS

Supporting Information

Characterizing the Geometry and Quantifying the Impact of Nanoscopic Electrocatalyst/Semiconductor Interfaces under Solar Water Splitting Conditions

*John R. Hemmerling, Aarti Mathur, and Suljo Linic**

Supporting Information

Characterizing the Geometry and Quantifying the Impact of Nanoscopic

Electrocatalyst/Semiconductor Interfaces Under Solar Water Splitting Conditions

John R. Hemmerling, Aarti Mathur, Suljo Linic

Section 1 Nanoparticle Electrodeposition Chronoamperometry

As described in the methods section, nickel nanoparticles were electrodeposited on the surface of n-type and p^+-type silicon wafer pieces housed in a 3-electrode setup. The focus of the electrodeposition recipe was to replicate the current density versus time plot shown below from sample to sample and for both types of silicon. The applied voltage was adjusted based on EIS measurements of each sample that determined the solution resistance and sample resistivity. The time was kept constant at 5 seconds of applied potential. Creating the chronoamperometry curve shown below allowed for a very uniform and precise distribution of nanoparticles on both types of silicon, creating a rigorous electrocatalyst control. The main features that needed to be reproduced in chronoamperometry by adjusting the voltage are the maximum current and the
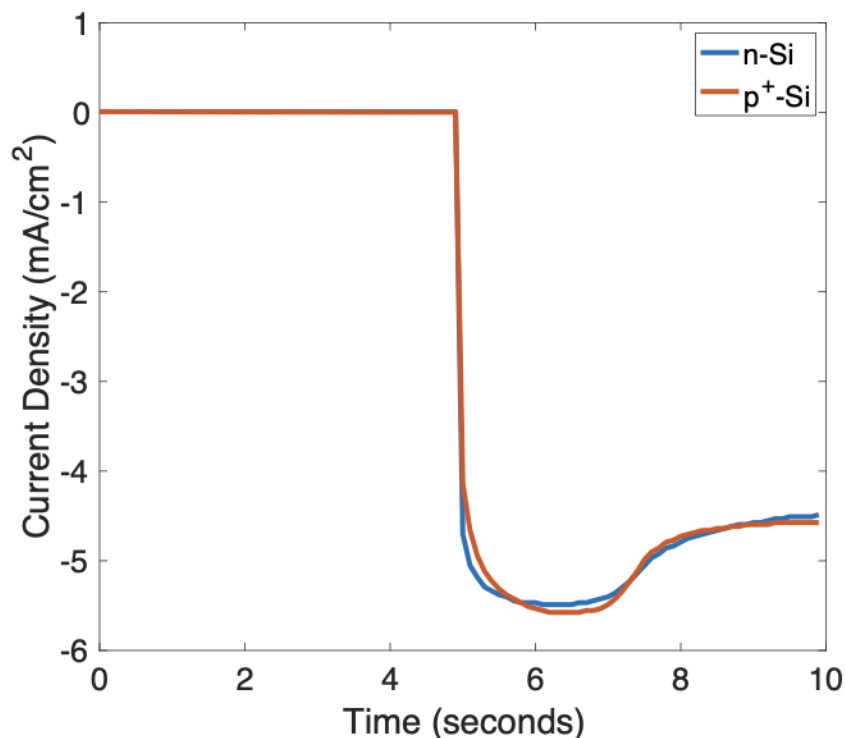
slope of the curve after reaching maximum current.

Figure S1 : Chronoamperometry plots for the Ni electrodeposition on n-Si and p+-Si. The samples are at open-circuit for the first 5 seconds before applying a reducing potential for 5 seconds of electrodeposition. The total applied voltage is typically more negative than -2 V vs Ag/AgCl and the selected voltage for a given sample depends on the resistance obtained from

EIS before the electrodeposition. After accounting for the ohmic losses, the target voltage applied to the working electrode is close to -1.5 V vs Ag/AgCl.

Section 2 Full Current Voltage Plots

The full current density-voltage (J-V) plots under 1-sun illumination for all samples are shown in Figure S2. The photo-limited current density for pf-Ni/SiO$_2$/n-Si (20.5 mA/cm^2) and np-Ni/n-Si (21 mA/cm^2) are very similar, meaning that the light transmission through the Ni overlayer is comparable despite the different architecture. While the Ni nanoparticles cover only about 21% of the Si surface, only a small fraction of the light can transmit through the relatively thick (> 40 nm diameter) nanoparticles. Meanwhile the thin planar Ni (~5 nm) enables a larger fraction of the light to transmit through the layer. We also note that the photo-limited current of pf-Ni/n-Si does not plateau but instead continues to increase with increasing voltage. This phenomena is due to the significant dark current that the system generates (in addition to the light current) because the barrier height is poor and allows for a significant shunt current. After subtracting the dark current, the measured photo-limited current density is 20.1 mA/cm^2, in good agreement with the other samples.
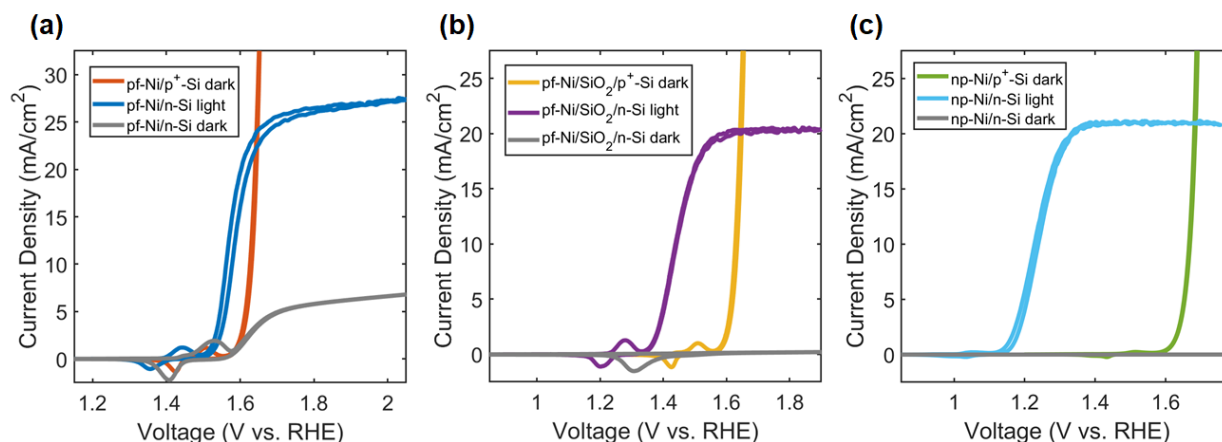
(a)

(b)

(c)

Figure S2: Full J-V plots for (a) pf-Ni/Si, (b) pf-Ni/SiO$_2$/Si, and (c) np-Ni/Si collected after 30 voltage sweeps. The curves for n-Si samples were collected under 1-sun illumination and in darkness, while p$^+$-Si electrocatalytic controls were collected in darkness.

Section 3 Additional SEM Characterization

SEM characterization of nanoparticle systems was used to analyze possible changes in the particle size distributions and nanoparticle coverage for np-Ni/n-Si samples throughout testing and exposure to oxidizing reaction conditions. SEM images were processed using IMAGEJ[1] by adjusting the threshold to only nanoparticles and remove SEM artifacts. The area of the nanoparticles was determined using the built in IMAGEJ particle analysis function with no filter on circularity or particle size. Particles clumped together were treated as one larger nanoparticle while nanoparticles with distinct edges were analyzed individually. The particle

radius was calculated from the area assuming a circular 2D geometry and the average particle radius was calculated over all analyzed areas.

Figure S3 contains a top-down visualization of np-Ni/n-Si before testing, after 5 cycles of cyclic voltammetry (CV) testing, and after 40 cycles of testing to evaluate if the nanoparticle size distribution changes significantly during testing. As seen in Figure S3, the size distribution does not change significantly which is consistent with our stable CV and photovoltage over time. The average nanoparticle radius increases slightly from 34.2 nm to 39.5 nm while apparent catalyst coverage increased from 22.1% to 22.9% catalyst coverage before and after electrochemical testing. These slight increases in size and coverage are consistent with the growth of an NiO_x shell surrounding the nanoparticles during exposure to the oxidizing potential sweeps.

SEM characterization of pf-Ni/SiO$_2$/Si nickel deposited as a planar layer on native silicon oxide is shown in Figure S4, with few surface defects present. Unlike the nanoparticle systems, the SEM images for the planar samples show minimal surface features indicating that the Ni film
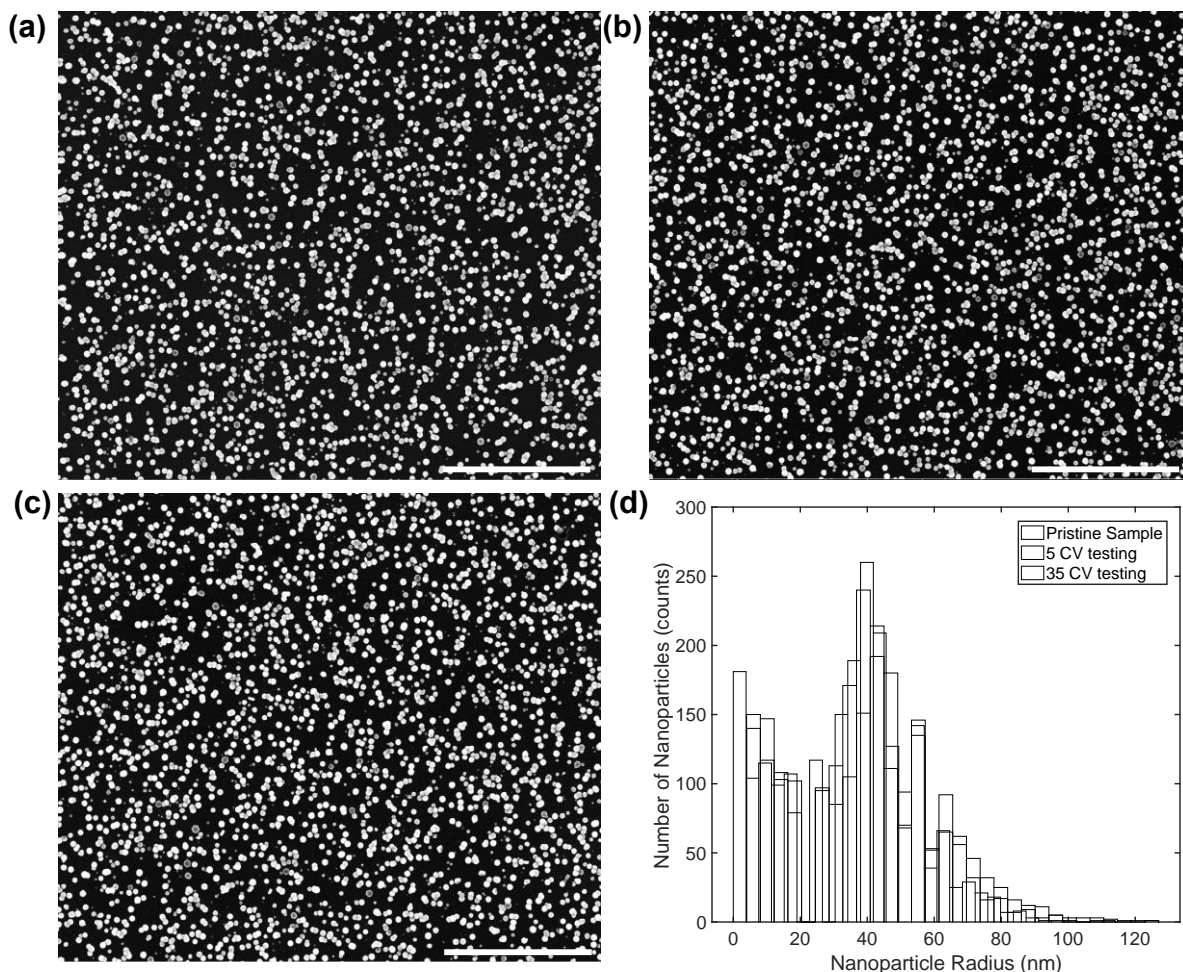
is planar and uniform.

Figure S3 (a)-(c) SEM images at 20kx magnification. The white scale bar represents 2 micrometers. (a) Pristine sample after electrodeposition of nickel nanoparticles, with a particle radius of 34.2±19.9nm and 22.1% coverage. (b) Image taken after 5 CV cycles, with a particle radius of 38.0±19.6 nm and 22.9% coverage. (c) Image taken after 40 CV cycles, with a particle

radius of 39.5±22.2 nm and 22.9% coverage. (d) Distribution of images a-c plotted as a function of nanoparticle radius.
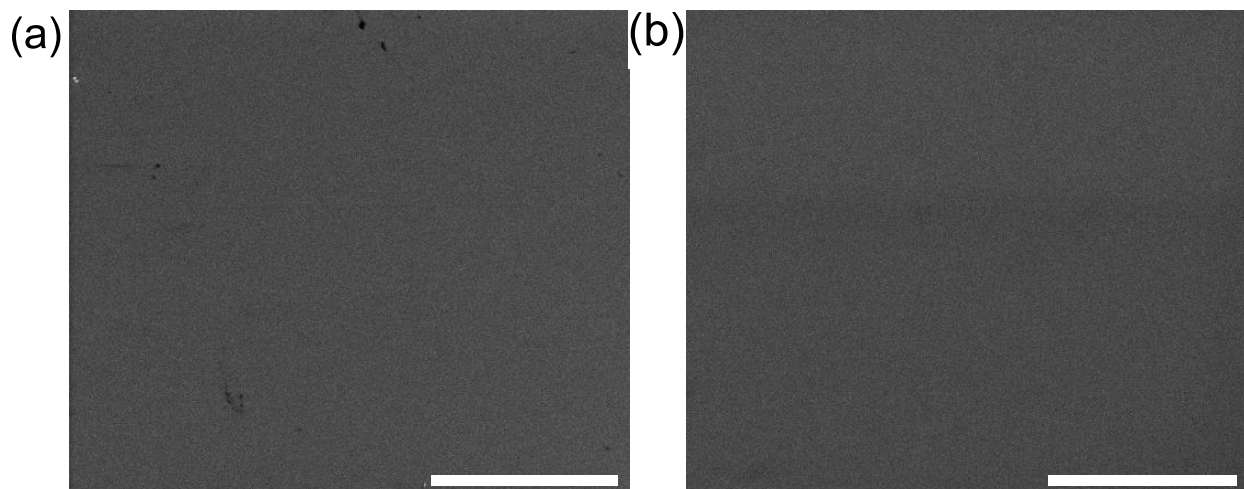

Figure S4: Top-down SEM image of planar nickel deposited on native silicon oxide. (a) scale bar represents 50 μm. (b) scale bar represents 5 μm.

Section 4 Long-term Cycling and Stability Testing

The np-Ni/n-Si samples were cycled using CV 260 times to gauge the long-term stability and evaluate catalytic activity and photovoltage over time. Figure S5a shows cycles 1 through
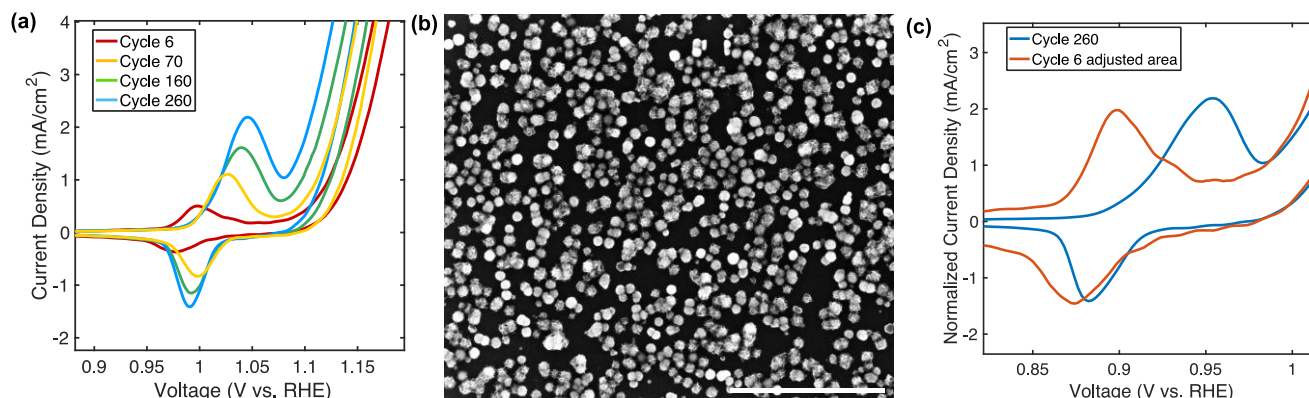
260 with increments at cycle 70 and 160. The onset potential at 1 mA/cm^2 continuously improves (i.e., shifts to more negative potentials) throughout the extended potential cycling. As stated in the main paper, the improvements are largely attributed to the gradual increase in the electrocatalytic active area from oxidation of the nanoparticle shell which is evident from the increased redox peaks over time. From charge integration of the forward-sweep redox peaks (and removing background capacitance), the active area of the oxidized nanoparticle shell increases by a factor of ~4 from cycle 6 to cycle 260. This means that the Ni nanoparticles activated for 260 cycles has ~4 times more active sites than a pristine catalyst. This increased active area results in a 56 mV improvement in the onset potential (Figure S5a). To confirm that this improvement primarily corresponds to the electrocatalytic active surface area, the CVs can be normalized to the active area. The onset potentials for cycle 6 and cycle 260 are nearly identical after normalizing to the electrocatalytic active surface area (such that both cases yield the same redox peak integration). This result indicates that (1) the photovoltage remains constant throughout the extended testing, despite extensive oxidation of the nanoparticles and (2) the onset potential shift can be largely attributed to increased electrocatalyst active area. We note that additional electrocatalytic improvements may also be attributed to iron incorporation from the electrolyte which can also explain the shift of the nickel redox peak to the right over long periods of time.[2] Figure S5b shows SEM imaging of the highly tested sample, where the increased oxidation is observed by a thicker average nanoparticle diameter and presence of fiber-like facets on nanoparticles.

Figure S5: (a) OER CVs throughout long-term cycling of np-Ni/n-Si showing cycles 6, 70, 160, and 260. The onset potentials significantly improve throughout the cycling experiments. (b) SEM imaging of nanoparticles after 260 cycles. 35kx magnification, scale bar represents 1um. (c) OER CVs for unmodified cycle 260 and cycle 6 multiplied by a factor of ~4 such that it has the same redox peak integration (active surface area) as cycle 260. After normalizing, the onset potentials converge to a similar value.

Section 5   Quantifying the Catalyst Contact Area and Interfacial Geometry

TEM analysis of np-Ni/n-Si both before and after testing indicated that the nanoparticle radius determined by top-down SEM was not indicative of the true EC/SC contact area. This is because the SEM top-down view can only measure the maximum radius of the nanoparticles but cannot observe the interfacial contact between the nanoparticle and semiconductor. To determine the corrected catalyst contact area, 25 nanoparticles were investigated, some of which are shown in Figure S6 a,b. Nanoparticles that overlap or are shadowed by a nanoparticle deeper in the sample were not included in the analysis. Nanoparticles were analyzed individually with high-resolution TEM images (like Figure 3a, b in the main text) to compare the nanoparticle/semiconductor contact radius ($r_{contact}$) and the nanoparticle maximum radius (r_{max}). The nanoparticle/semiconductor contact radius is defined by the region in which pure Ni is in closest contact to the Si. All of the charge carrier transfer is assumed to occur through the pure metallic Ni, and therefore the less conductive NiO_x region is not included in the contact radius. The ratio of the nanoparticle contact radius to the maximum diameter ($\frac{r_{contact}}{r_{max}}$) was averaged for the 25 nanoparticles, and this average ratio was used to measure the fraction of the semiconductor surface in direct contact with the catalyst (f_c):

$$f_c = f_{c,SEM} \left(\frac{r_{contact}}{r_{max}} \right)^2 \qquad\qquad \text{S1}$$

Here, $f_{c,SEM}$ is the catalyst coverage as determined from the SEM top-down imaging. We note that $f_{c,SEM}$ is an important consideration for light absorption and transmission, but f_c is important for the charge transfer and recombination at the nanoparticle/semiconductor interface (equation 3 in the main text).

Figure S6c,d shows high resolution TEM images of the nickel nanoparticle/silicon interface, with the silicon crystal lattice visible. All samples imaged using TEM for EDS or nanoparticle contact area measurements were aligned to the silicon <100> plane using a double tilt holder. This alignment ensured that the sample was being imaged perpendicular to the interface, and that all measurements of interface thickness were accurate. The high-resolution STEM images illustrate the 4 distinct layers at the interface: Si substrate, SiO_2 insulator layer (~2.3 nm thick), NiO_x layer (~2.4 nm thick), and Ni nanoparticle overlayer.
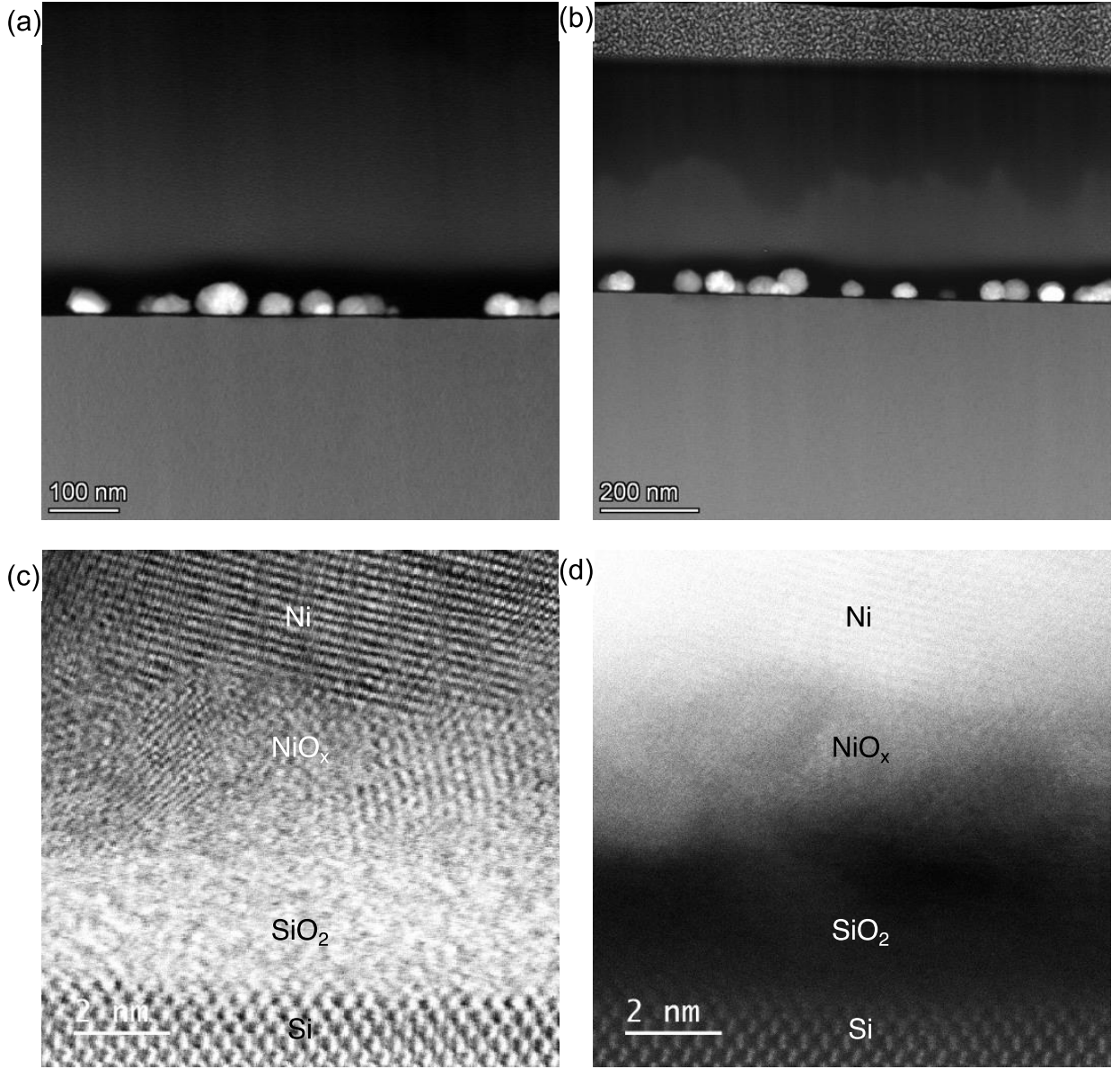
Figure S6: (a, b) Low-magnification TEM images of a few of the tested nickel nanoparticles used to determine the contact radius to maximum particle radius ratio. (c, d) High-magnification TEM images of silicon/nickel nanoparticle interface.

Section 6   Mott-Schottky Analysis to Extract the Ideal Barrier Height

For the pf-Ni/SiO₂/n-Si samples, the flat-band potential was measured using the Mott-Schottky equation:

$$\left(\frac{1}{C_{sc}}\right)^2 = \frac{2}{\varepsilon_0 \varepsilon_s A^2 q N_D}\left(V_a - V_{fb} - \frac{kT}{q}\right) \qquad \text{S2}$$

Where C_{sc} is the capacitance of the space charge region in the semiconductor, ε_0 is the vacuum permittivity, ε_s is the semiconductor relative permittivity, A is the surface area of the junction, N_D is the doping density of the semiconductor, V_a is the applied voltage relative to the redox potential of the electrolyte, V_{fb} is the flat-band potential, k is the Boltzmann constant, T is the temperature, and q is the elementary charge of an electron.

C_{sc} is measured using electrochemical impedance spectroscopy (see methods) and fitting the data to the equivalent circuit shown in the inset of Figure S7 using previously described methods.[3,4] Data in Figure S7 shows a representative Mott-Schottky plot for the pf-Ni/SiO$_2$/n-Si sample. The resulting flat-band potential is 0.46 eV, and the doping density is 7.6e15 cm^{-3} which is in good agreement with 4-point probe measurements (7.5e15 cm^{-3}) taken on the pristine Si before fabrication. This doping density is related to the potential difference or offset between the semiconductor conduction band and the semiconductor Fermi level (V_n) by the following equation:

$$V_n = V_{fb} + \frac{kT}{q} ln \frac{N_C}{N_D} \qquad\qquad \text{S3}$$

Where N_C is the effective density of states in the Si conduction band. Then the ideal barrier height ($\phi_{b,ideal}$) is given by the following equation:

$$\phi_{b,ideal} = V_{fb} + V_n \qquad\qquad \text{S4}$$

The barrier height evaluated from the flat-band potential is considered the ideal barrier height (also known as the flat-band or Mott-Schottky barrier height) because it is the maximum barrier height for a system if it were to behave ideally (i.e., if the ideality factor was 1). This is because at the flat-band potential, there is no electric field in the semiconductor, whereas the influence of nonidealities is dependent on an electric field. For example, a common source of nonidealities are defect states at interfaces. These defects cannot be charged in the absence of an electric field and therefore cannot contribute to the ideality factor at the flat-band potential.[3,5] However, it is important to note that water splitting systems operate under electric fields, so nonidealities can lower the barrier height for operating systems (see next section).

From the Mott-Schottky analysis, the measured values for V_n and $\phi_{b,ideal}$ for pf-Ni/SiO$_2$/Si are 0.21 eV and 0.67 eV, respectively. For np-Ni/n-Si samples, these parameters cannot be reliably measured using the Mott-Schottky method due to the inhomogeneous nature of the interfaces (nanoparticle vs electrolyte junctions). The Ni nanoparticle/Si junction is assumed to have the same properties as measured for the pf-Ni/SiO$_2$/Si sample, and this assumption has been justified in the main text and in Supplemental Sections 7, 8, and 9. We also note that for pf-Ni/n-Si systems, V_{fb} and $\phi_{b,ideal}$ cannot be directly measured from the Mott-Schottky plots because the barrier height is very low, resulting in inaccurate measurements of the space charge capacitance. Instead, these parameters are measured using the procedure described in Supplemental Section 7.
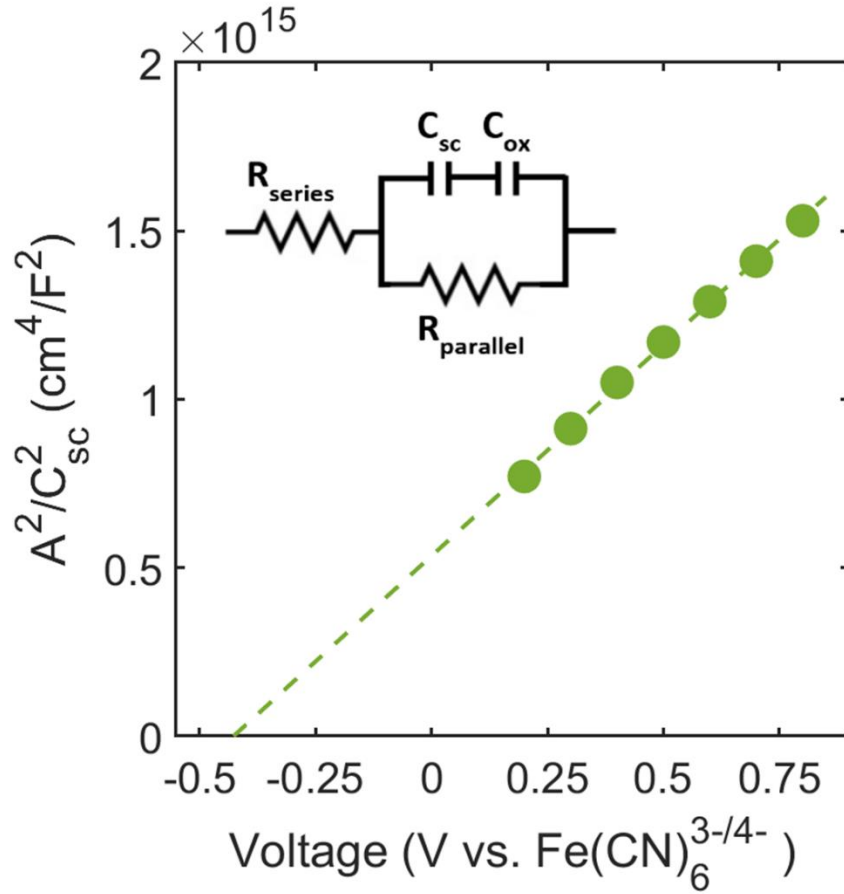
Figure S7: Representative Mott-Schottky plot of a pf-Ni/SiO$_2$/Si sample measured in the dark in a ferri/ferrocyanide redox couple. The inset shows the equivalent circuit used to fit the impedance data.

Section 7 Varying Light Intensity to Measure Barrier Height and Ideality Factor

Varying the light intensity (i.e., varying the photo-limited current) is based on the relationship between open-circuit photovoltage (V_{oc}) and the photo-limited current density (J_{ph}) which can be obtained from the diode equation (equation 1 in the main text) by setting the net-current (J_{net}) to zero and assuming that $\frac{J_{ph}}{J_s} \gg 1$:[6]

$$V_{oc} \approx \frac{nkT}{q} ln(J_{ph}) - \frac{nkT}{q} ln(J_s) \qquad \text{S5}$$

Based on this equation, then a plot of V_{oc} vs $ln(J_{ph})$ will yield a straight line with a slope that is related to the ideality factor and an intercept that is related to the saturation recombination current (J_s).[3,7] The results of these experiments for the pf-Ni/n-Si and pf-Ni/SiO$_2$/n-Si systems are provided in Figure S8.

Interestingly, pf-Ni/n-Si is close to ideal ($n = 1.026$) while pf-Ni/SiO$_2$/n-Si is highly nonideal ($n = 1.778$). An ideality factor close to unity is common for direct metal-semiconductor

Schottky contacts, and slight deviations from unity are typically associated with image force lowering or inhomogeneous interfaces.[8–10] The nonidealities for pf-Ni/SiO$_2$/n-Si are commonly attributed to interfacial defect states which result in an insulator voltage drop.[3,11]
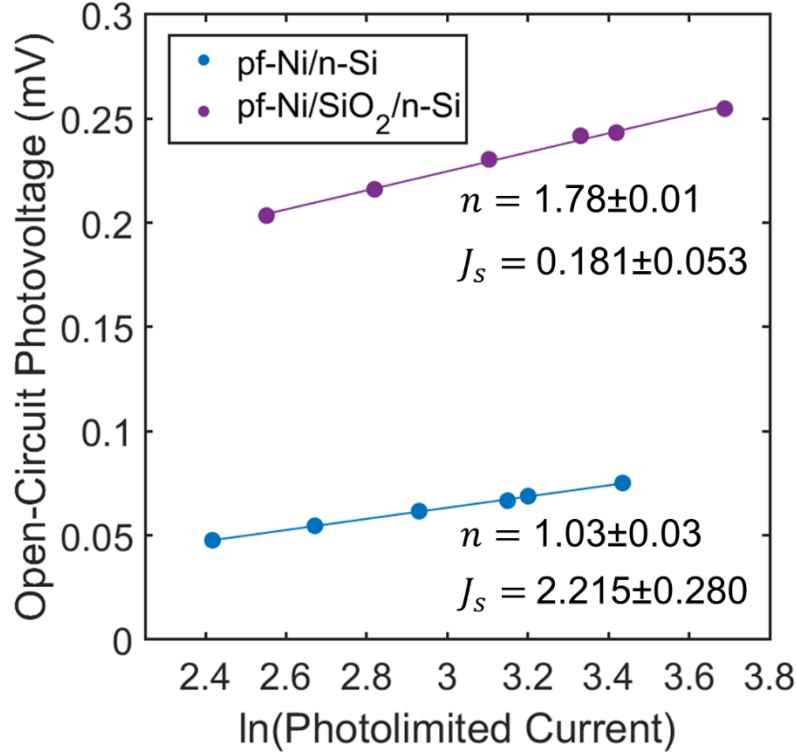

Figure S8: Results of the light intensity experiments in which the open-circuit photovoltage is measured as a function of the natural log of the photo-limited current density. pf-Ni/n-Si samples exhibited a high dark current, so the photo-limited current was obtained by subtracting the dark current from the light current. We also note that equation S5 is valid when $\frac{J_{ph}}{J_s} \gg 1$ which may not be strictly true for pf-Ni/n-Si samples and therefore results in a larger degree of uncertainty in the reported values. This is not a concern for pf-Ni/SiO$_2$/n-Si samples because the dark recombination current is an order of magnitude lower.

The data in Figure S8 show that J_s is about an order of magnitude lower for pf-Ni/SiO$_2$/n-Si compared to pf-Ni/n-Si. This difference is largely attributed to the native oxide which decreases recombination rates through the tunneling probability term (see equation 3 from the main text). To quantify the specific differences between pf-Ni/SiO$_2$/n-Si and pf-Ni/n-Si, the barrier heights and tunneling probabilities must be evaluated. For pf-Ni/n-Si, without any interfacial insulator layer, the barrier height can be directly measured using equation 2 from the main text. The resulting barrier height for pf-Ni/n-Si is 0.57 eV (Figure S9). ϕ_b is defined as the barrier height when the system is in equilibrium (i.e., no applied voltage, $V = 0$). This ϕ_b is distinct from the ideal flat-band barrier height ($\phi_{b,ideal}$) which is defined when the system is at the flat-band potential (i.e., $V = V_{fb}$). It has been shown that $\phi_{b,ideal}$ is related to ϕ_b by the following expression:[5]

$$\phi_{b,ideal} = n\phi_b - (n-1)V_n \qquad\qquad\qquad S6$$

Since n, ϕ_b, and V_n are known for pf-Ni/n-Si, $\phi_{b,ideal}$ can be readily calculated, and it is reported in Figure S9. In contrast to pf-Ni/n-Si, ϕ_b for pf-Ni/SiO$_2$/n-Si cannot be directly extracted from J_s (equation 3 in the main text) because it contains contributions from both the barrier height and the SiO$_2$ tunneling probability which must be deconvoluted. Instead, ϕ_b is determined by using $\phi_{b,ideal}$ and V_n measured from the Mott-Schottky method in Section 6 and using n from Figure S8. For this calculation equation S6 is rearranged to solve for ϕ_b :

$$\phi_b = \frac{\phi_{b,ideal}}{n} + \left(\frac{n-1}{n}\right) V_n \qquad\qquad \text{S7}$$

From equations S6 and S7, it is evident that $\phi_b = \phi_{b,ideal}$ when a system is ideal (n=1), and that $\phi_b < \phi_{b,ideal}$ when the system is nonideal (n >1). In other words, the presence of nonidealities, regardless of their origin, results in a lowering of the barrier height.

The compiled barrier heights for pf-Ni/n-Si and pf-Ni/SiO$_2$/n-Si are reported in Figure S9. For pf-Ni/n-Si, the ideal barrier height ($\phi_{b,ideal}$) and equilibrium barrier height (ϕ_b) are very similar because the system is nearly ideal ($n = 1.03$). In contrast, pf-Ni/SiO$_2$/n-Si is less ideal ($n = 1.78$) which results in ϕ_b being significantly lower than $\phi_{b,ideal}$. Overall, the presence of nonidealities results in a ϕ_b for pf-Ni/SiO$_2$/n-Si that is even lower than ϕ_b for pf-Ni/n-Si. Even though pf-Ni/SiO$_2$/n-Si has a lower equilibrium barrier height, the overall recombination current (J_s in Figure S8) is an order of magnitude lower compared to pf-Ni/n-Si which must be due to the tunneling probability term (T_t from equation 3 in the main text). In other words, the enhanced tunneling probability offered by the SiO$_2$ layer in pf-Ni/SiO$_2$/n-Si more than compensates for the lower barrier height which ultimately leads to lower recombination and higher generated photovoltage. The strategy to evaluate the role of the SiO$_2$ layer is described in Section 11.
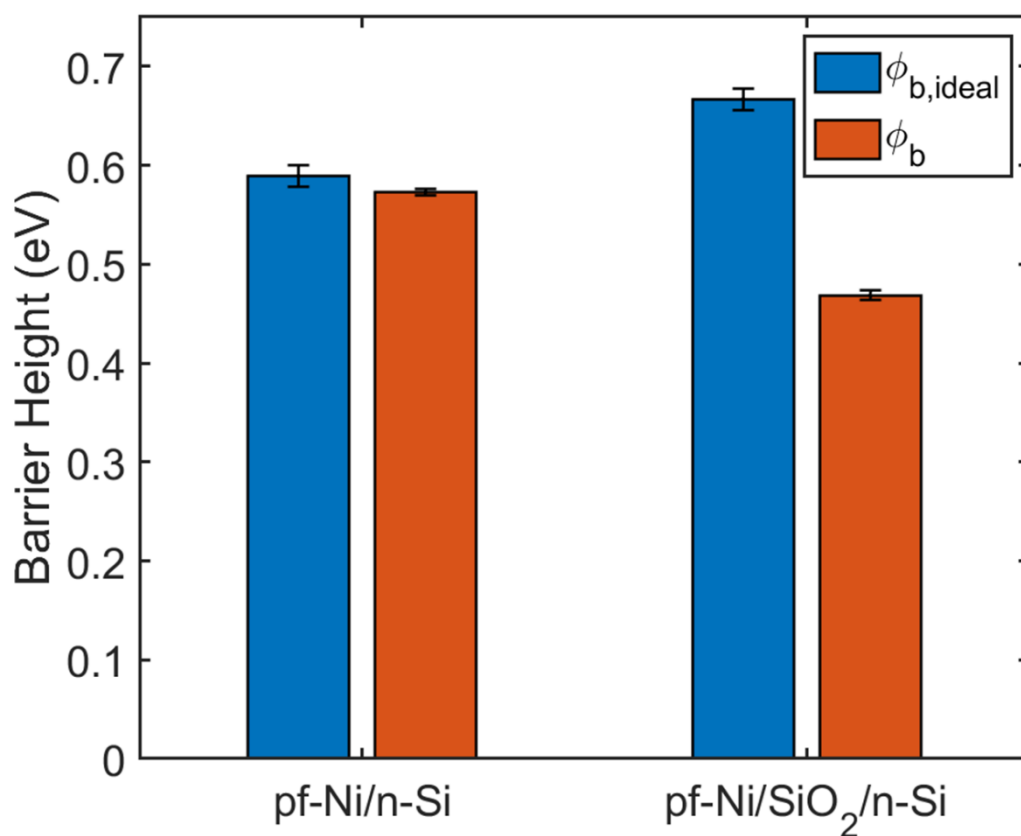
Figure S9: Compiled ideal barrier heights ($\phi_{b,ideal}$) and equilibrium barrier heights (ϕ_b) for pf-Ni/n-Si and pf-Ni/SiO$_2$/n-Si samples. For pf-Ni/n-Si, $\phi_{b,ideal}$ and ϕ_b was measured using equation S6 and using J_s from the light intensity experiments, respectively. For pf-Ni/SiO$_2$/n-Si, $\phi_{b,ideal}$ and ϕ_b was measured using the Mott-Schottky method and using equation S7, respectively. np-Ni/n-Si (not shown) is assumed to have the same barrier height characteristics as pf-Ni/SiO$_2$/n-Si.

Section 8 Evaluating the Role of Thin Interfacial NiO$_x$

Based on the STEM cross-sectional imaging, the np-Ni/n-Si samples includes an oxidized Ni layer (NiO$_x$) between the Ni np and the SiO$_2$ and Si. Previous reports and modeling efforts do not analyze this interfacial layer or assume that the Ni nanoparticles result in a lower barrier direct Ni/Si contact.[12–15] However, it is possible that the interfacial NiO$_x$ could impact the barrier height due to its high work function which may exceed 5 eV.[16–18] We note that this is distinct from other reports suggesting that a high work function NiO$_x$ shell around the nanoparticle pinches off the nanoparticle to induce a larger effective barrier height.[12,13,19–21] We discuss this possibility in Section 9.

To investigate the role of the interfacial NiO$_x$, we fabricated planar Ni/NiO$_x$/SiO$_2$/Si systems. 2 nm of planar Ni was deposited on n-Si or p$^+$-Si with native oxide, and the Ni layer was oxidized by repeated cycling in KOH. The photovoltage over time was evaluated using a 2nm-Ni/SiO$_2$/p$^+$-Si control sample, and the results are shown in Figure S10. Compared to the 5nm-Ni sample, the 2 nm Ni sample has about 100 mV higher photovoltage (up to 340 mV).

This general improvement in the photovoltage using thinner Ni has been previously reported; however, the photovoltage decreases as the Ni oxidizes which is in contrast to previous reports.[22,23] The fact that the photovoltage drops over time (even as the Ni oxidizes and the electrocatalytic activity improves) suggests that the formation of NiO_x does not improve the system's barrier height, and may even lower the barrier height. There are several forms of NiO_x with different work functions, which may explain the differences with previous reports.[16–18] The potential cycling was continued until the sample became highly resistive, indicating that the conductive Ni film had been oxidized to more resistive NiO_x.

After oxidizing the 2nm-Ni/SiO_2/n-Si sample, 20 nm of planar Ni was deposited to form a 20nm-Ni/2nm-NiO_x/SiO_2/n-Si which simulates the behavior of a Ni nanoparticle with 20 nm diameter and a 2 nm NiO_x interfacial layer. A control sample of 20nm-Ni/SiO_2/n-Si without the NiO_x interfacial layer was also fabricated. The CVs in Figure S11a in a ferri/ferrocyanide electrolyte shows that the 20nm-Ni/2nm-NiO_x/SiO_2/n-Si sample with interfacial NiO_x is highly resistive despite the addition of a 20 nm thick conductive Ni layer. This analysis suggests that a fully oxidized NiO_x layer at the interface results in increased resistance and loss of photovoltage, rather than improved performance. Because high resistance is not observed in np-Ni/Si, it can be concluded that the evolved interfacial NiO_x underneath nanoparticles is thin enough and conductive enough to minimize resistance losses.
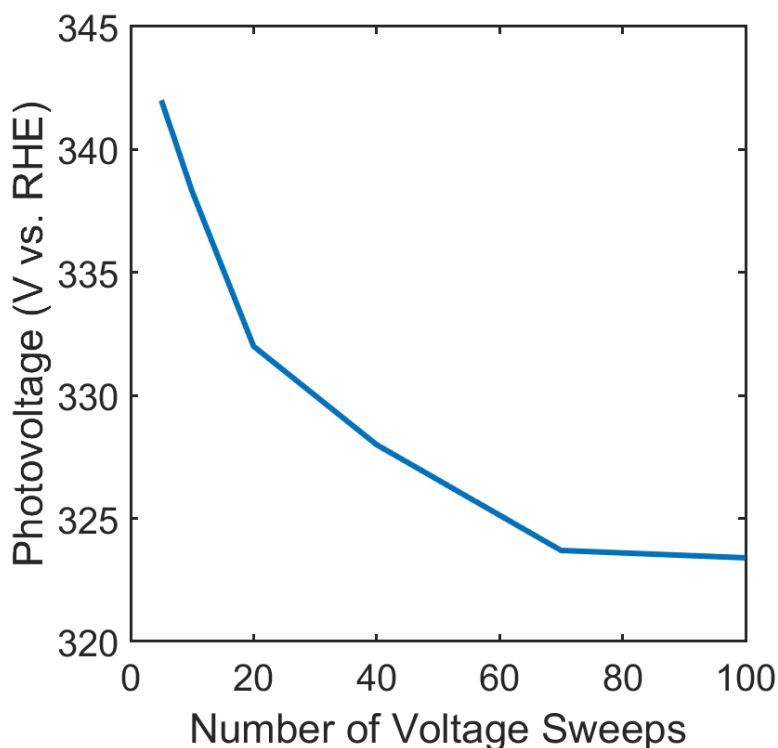

Figure S10: Photovoltage degradation over time for the 2nm-Ni/SiO_2/n-Si

Figure S11a shows the flat-band potentials for each system. The presence of interfacial NiO_x results in a slightly lower flat-band potential and barrier height, indicating that the effective work function of the NiO_x/Ni contact is lower than the pure Ni contact. This analysis suggests interfacial NiO_x has a slight detrimental effect on the barrier height of the system, but the overall

barrier height is dominated by the thick Ni layer. Indeed, such a thin NiO_x layer (~2 nm) underneath a >20 nm Ni np overlayer is expected to have a negligible impact on the effective work function and barrier height of the junction because the thick overlayer tends to dominate the junction characteristics, especially when there is considerable interdiffusion between the layers.[24] Overall, these results support the conclusion that a thin NiO_x layer evolved at the interface during OER electrochemical cycling does not significantly impact the barrier height of the junction.
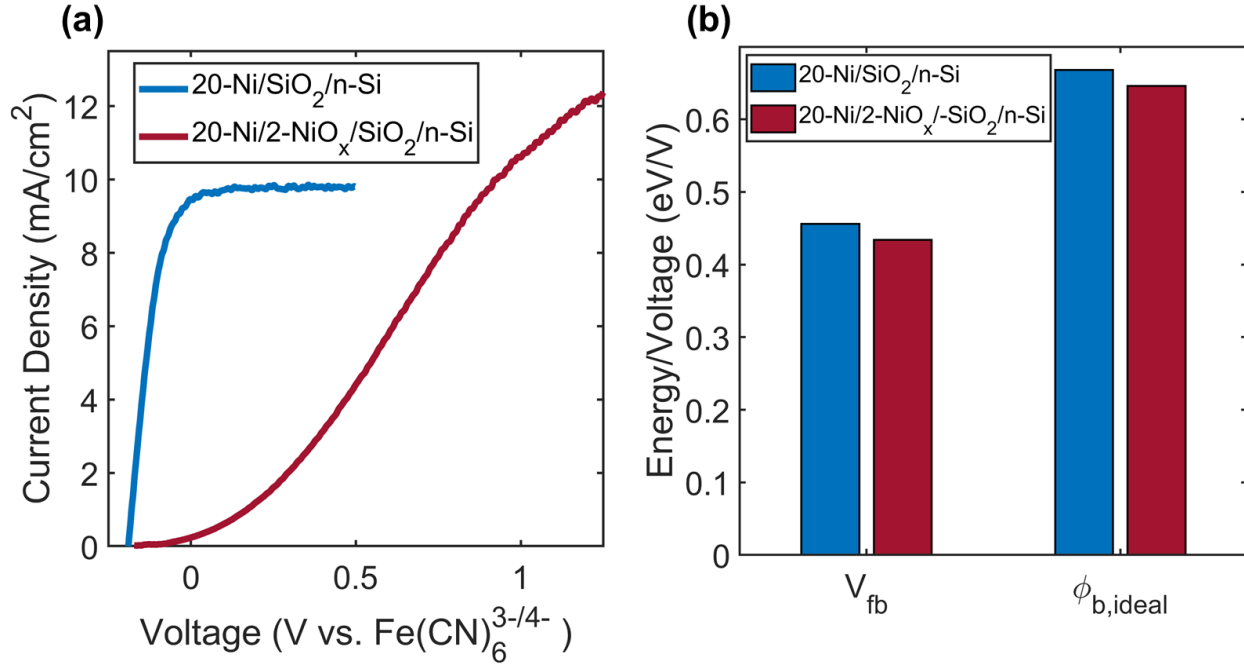

(a)

(b)

Figure S11: (a) CVs in 350/50 mM ferri/ferrocyanide and 1 M KCl electrolyte under approximately 1-sun illumination. The curves are corrected for solution resistance and the dark current was subtracted. (b) Measured flat-band potentials and ideal barrier heights for 20nm-Ni/2nm-NiO_x/SiO_2/n-Si and 20nm-Ni/SiO_2/n-Si

Section 9   COMSOL Multiphysics[®] Modeling of the pinch-off effect

The high photovoltages of nanoparticle systems is commonly attributed to the so-called "pinch-off effect".[9,25] Specifically, it has been proposed that the evolution of a high work function NiO_x shell surrounding the nanoparticle increases the effective barrier height of the nanoparticle.[12,13,19–21] To determine if the pinch-off effect increases the effective barrier height and photovoltage for our experimental systems, we modeled the nanoparticle systems using COMSOL Multiphysics[®]. In short, the model is based on cylindrical Si with axial symmetry, and a low-barrier nanoparticle is placed on the Si and surrounded by a high-barrier shell (Figure S12). The dimensions of the contact area and shell thickness are based on the cross-sectional STEM analysis. The baseline case is a 30 nm Ni contact radius surrounded by a 3 nm shell which is comparable to the experimental observations, and a sensitivity analysis with higher and lower values was also performed. We note that the model is designed to capture the upper-bound on the pinch-off effect by (1) removing all other sources of recombination besides thermionic emission recombination under the nanoparticle contact (i.e., the system is ideal and therefore the ideal barrier height of 0.67 eV is used for the nanoparticle junction; if the system was non-ideal, then

the barrier height would be decreased (equation S7) and lower the photovoltage), (2) using the upper limit for the NiO$_x$ shell's barrier height of 1.1 eV which is equal to the band gap of Si, and (3) minimizing resistance losses.
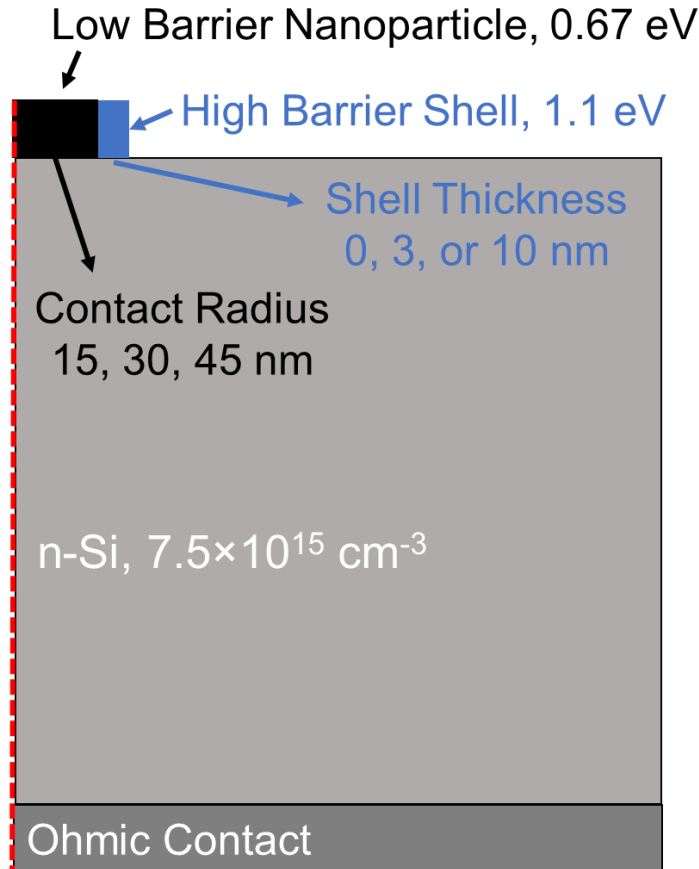

Figure S12: Schematic of the model geometry used for COMSOL simulations. The total dimensions of the Si is 1x1 μm, which is big enough to fit the entire space charge region, but small enough to minimize resistance losses. The radius of the nanoparticle was varied between 15, 30, or 45 nm with a barrier height of 0.67 eV. The NiO$_x$ shell surrounding each nanoparticle varied between a thickness of 0, 3, or 10 nm with a barrier height of 1.1 eV (work function of 5.15 eV). In the top plane of the system, charge is only allowed to conduct through the nanoparticle contact and no charge passes through the NiO$_x$ shell. The Si doping density is 7.5e15 cm^{-3} which corresponds to resistivity of about 0.68 ohm-cm similar to the experimental Si used in this study. The backside of the Si is modeled as an ideal ohmic contact. The red dashed line marks the axis in which the system is rotated with axial symmetry. No interfacial SiO$_2$ layer or tunneling contributions are included in the model.

Data in Figure S13 show the modeled potential barrier in the Si for nanoparticle systems with different nanoparticle radii and different shell thicknesses. In all cases, an increase in the oxide shell thickness results in a wider potential barrier but has negligible impact on the barrier height. The height, not the width, of the barrier is the key parameter governing the photovoltage. Indeed, we find that the oxide shell, and therefore the pinch-off effect, has only a tiny impact on

the generated photovoltage. We calculate the photovoltage of each system using the J-V plots from COMSOL and using the experimental photo-limited current of 21 mA/cm^2 and catalyst coverage of 10%. To confirm the validity of the COMSOL model, we measured the photovoltage for nanoparticles without any NiO$_x$ shell (i.e., no pinch-off effect), and the generated photovoltage was 215 mV which was independent of nanoparticle size (assuming constant catalyst surface coverage (f_c) of 10%. As expected, this COMSOL photovoltage of 215 mV is in close agreement with the analytical model (equations 1 and 2 from the main text using $f_c = 10\%$, $J_{ph} = 21$ mA/cm^2, and $\phi_b = 0.67$ eV) which yielded a photovoltage of 214 mV.

For the baseline case of a 30 nm contact radius and 3 nm NiO$_x$ shell, the photovoltage is only enhanced by 2 mV relative to systems without any NiO$_x$ shell (217 mV compared to 215 mV for the same catalyst coverage of 10%). For the most extreme case of a 15 nm contact radius surrounded by a 10 nm shell, the photovoltage only increased by 20 mV up to 235 mV. This analysis indicates that even the smallest nanoparticles with radius of 15 nm will not be significantly impacted by an NiO$_x$ shell via the pinch-off effect.

We emphasize that the COMSOL model was designed to obtain the upper bounds on the pinch-off effect by choosing the upper limit for the NiO$_x$ shell's barrier height of 1.1 eV (which results in the highest possible band bending equal to the Si band gap). In reality, the performance is expected to be even lower than the models predict. Overall, these modeled photovoltages (<250 mV) based on the pinch-off effect are much lower than the experimental photovoltages (>450 mV), meaning that the pinch-off effect as previously described in the literature (i.e., a high barrier shell surrounding a low barrier nanoparticle) fundamentally cannot explain the high performance achieved by np-Ni/n-Si. This analysis demonstrates that a NiO$_x$ shell does not impact the overall barrier height of the junction or enhance the photovoltage. These results are consistent with the fact that the experimental photovoltages remain stagnant (Figure 2 in the main text) even as the NiO$_x$ shell continuously evolves during electrochemical testing.

(a)   **(b)**   **(c)**
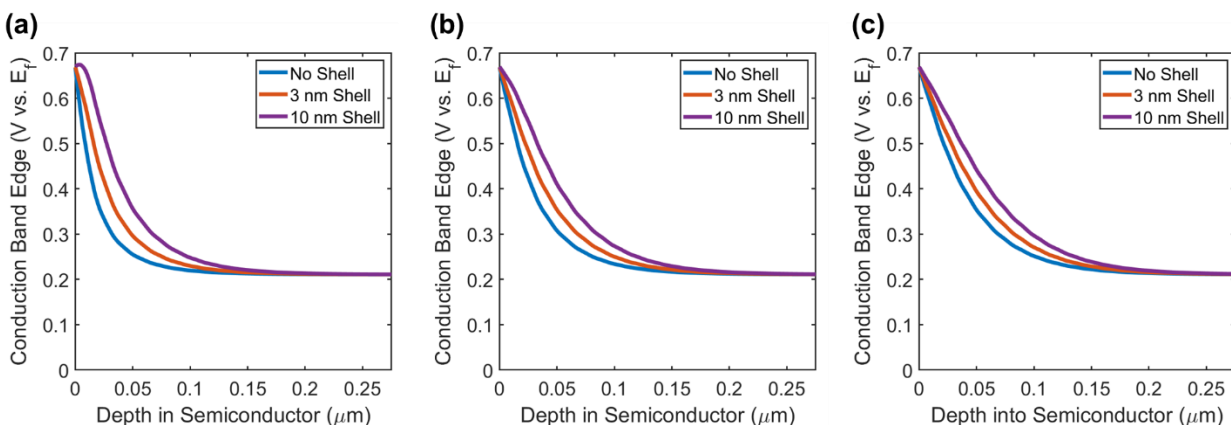
Figure S13: Modeled conduction band edges and potential barriers for different NiO$_x$ thicknesses for nanoparticle sizes of (a) 15 nm, (b) 30 nm, and (c) 45 nm.

Section 10 Modeling J-V Plots

The following procedure is followed to model the J-V plots:

1. Create a Tafel plot of the IR-compensated experimental p$^+$-Si samples to measure the electrocatalyst exchange current density ($J_{o,cat}$) and the Tafel slope (b). To model the J-V relationship for the electrocatalyst p$^+$-Si control samples, use the anodic part of the Butler-Volmer equation:

$$J_{cat} = J_{o,cat} \left[exp \left(\frac{V_{cat}}{b} \right) \right]$$

Where J_{cat} is the catalytic current density and V_{cat} is the catalytic overpotential relative to the redox potential of the OER. This equation is sufficient to model the J-V relationship of the electrocatalyst. It matches the electrocatalyst p$^+$-Si control samples very well if the Tafel slope is constant throughout the potential range and if the series resistance has been subtracted (IR-compensated).

2. Perform light intensity experiments to measure the dark saturation recombination current (J_s) and the ideality factor (n) for the n-Si samples.
3. Measure the photo-limited current density (J_{ph}) for the n-Si samples under 1-sun illumination.
4. Use the diode equation to model the J-V characteristics of the photovoltage-generating junction:

$$J_{diode} = J_{ph} - J_s \left[exp \left(-\frac{qV_{diode}}{nkT} \right) - 1 \right]$$

5. Both the catalytic current and the photovoltage-generating diode or solar cell component have been modeled. In photoelectrochemical systems, the current through the solar cell diode junction is in series with the electrocatalytic current. Therefore, the total current (J_{total}) through the system is equal to the current through each component:

$$J_{total} = J_{cat} = J_{diode}$$

This also means that the voltages through each component will be additive:

$$V_{total} = V_{cat} + V_{diode}$$

6. J_{total} is incrementally varied and for the value for V_{cat} and V_{diode} is solved at each increment using equations S8 and S9. Then the total voltage is modeled as a function of current using equation S11. This process yields the J-V plot for n-Si systems which accurately match the experimental data (Figure 4 and Figure S14).
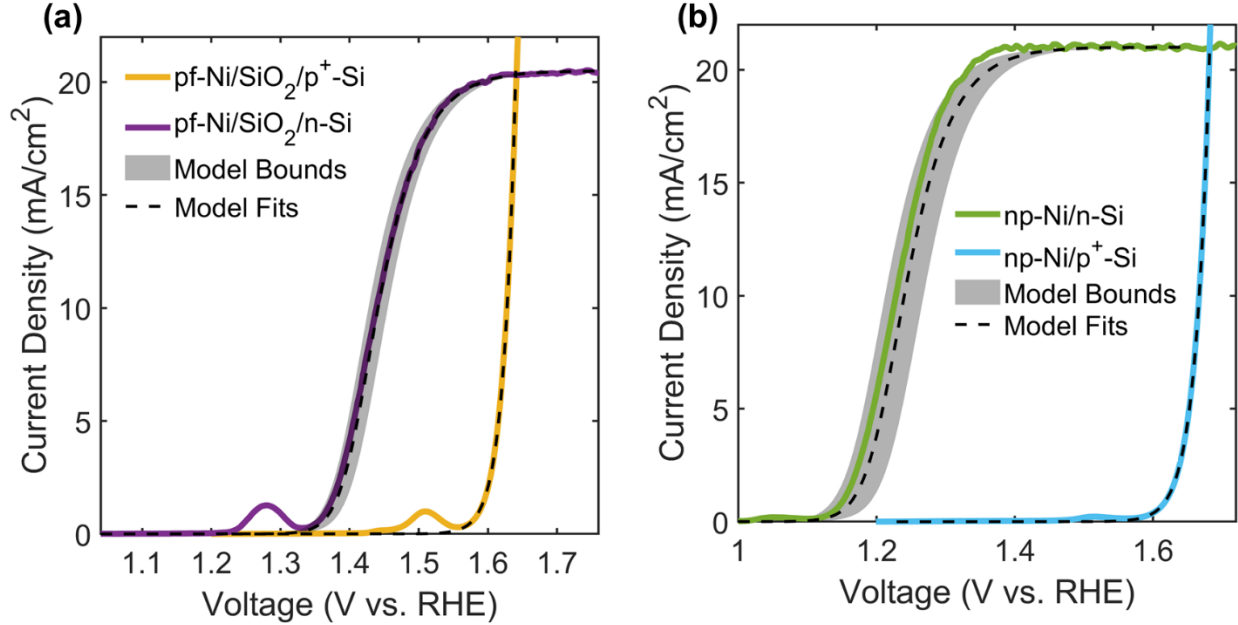
Figure S14: Experimental J-V forward sweeps overlaid with the corresponding modeling results for (a) pf-Ni/SiO$_2$/Si and (b) np-Ni/Si. The shaded region represents the upper and lower bounds (plus and minus 1 standard deviation) of the modeling results based on the uncertainties of the experimentally measured parameters. For np-Ni/n-Si, the modeled results match the slope and fill factor of the experimental result. This further validates the assumption that both np-Ni/n-Si and pf-Ni/SiO$_2$/n-Si have the ideality factor. If instead an ideality factor of 1 were assumed, the slope and fill factor the model would not match the experimental data.

Section 11 Methodology to Quantify the Tunneling Probability Term

The following procedure is followed to quantify the tunneling probability term for pf-Ni/SiO$_2$/n-Si:

1. Measure the flat-band potential (V_{fb}) and the doping density (N_d and V_n) using the Mott-Schottky method.
2. Use equation S4 to calculate the ideal barrier height ($\phi_{b,ideal}$).
3. Perform light intensity experiments to measure the dark saturation recombination current (J_s) and the ideality factor (n).
4. Use equation S7 to calculate the barrier height (ϕ_b).
5. Now that ϕ_b and J_s are known, use equation 3 from the main text to calculate the tunneling probability term, $T_t = \exp\left(-\propto d\sqrt{\phi_e}\right)$.
6. Measure the SiO$_2$ thickness (d) from STEM cross-sectional analysis.
7. Now the insulator conduction band offset (ϕ_e) can be quantified from the tunneling probability term, assuming that $\propto$ is unity.[11]

Section 12 Key Model and Experimental Parameters and Values
Table S1: Key experimental parameters for n-type samples

Parameter	Symbol	pf-Ni/n-Si	pf-Ni/SiO$_2$/n-Si	np-Ni/n-Si
Expt. Photovoltage (mV)	V_{ph}	65±4	230±10	480±12
Model Photovoltage (mV)	V_{ph}	62±4	220±12	456±28
Photo-limited Current	J_{ph}	20.1±0.4	20.5±0.3	21±0.5
Onset Potential (V vs. RHE)	V_{onset}	1.521±0.004	1.355±0.010	1.144±0.012
Si Potential Offset (meV)	V_n	0.211±0.002*	0.211±0.002	0.211±0.002*
Flat-band Potential (meV)	V_{fb}	NA	0.456±0.012	NA
Ideal Barrier Height (eV)	$\phi_{b,ideal}$	0.589±0.011	0.667±0.011	0.667±0.011*
Dark Saturation Current (mA/cm^2)	J_s	2.215±0.280	0.181±0.053	(9.5±5.8)×10^{-4}*
Ideality Factor	n	1.03±0.29	1.77±0.01	1.77±0.01*
Equilibrium Barrier Height (eV)	ϕ_b	0.573±0.003	0.455±0.005	0.455±0.005*
SiO$_2$ Thickness (nm)	d	NA	1.60±0.14	2.31±0.28
Insulator Tunneling Barrier (eV)	ϕ_e	0	0.171±0.020	0.171±0.020*
Tunneling Probability	T_t	1	(1.4±0.5)×10^{-3}	(7.2±1.7)×10^{-5}*
Nanoparticle Max Radius (nm)	r_{max}	NA	NA	35.7±18.7
Ratio of Nanoparticle Contact Radius to Max Radius	$\dfrac{r_{contact}}{r_{max}}$	NA	NA	0.70±0.08
Nanoparticle Contact Radius (nm)	$r_{contact}$	NA	NA	25.07±13.43
Catalyst Top-down Coverage (%)	$f_{c,SEM}$	1	1	20.68±0.32
Catalyst Close Contact Coverage (%)	f_c	1	1	10.17±1.15

*Values were not directly experimentally measured and are instead based on the assumption that the values for those specific parameters are identical to the values experimentally measured for pf-Ni/SiO$_2$/n-Si, which has been justified throughout the text.

Table S2: Key model and experimental values for p-type electrocatalytic controls after 30 potential sweeps

Parameter	Symbol	pf-Ni/p$^+$-Si	pf-Ni/SiO$_2$/p$^+$-Si	np-Ni/p$^+$-Si
Tafel Slope (mV/decade)	b	40.5	40.5	47.0
Exchange Current Density (mA cm^{-2})	$J_{o,cat}$	1.42×10^{-9}	1.42×10^{-9}	4.82×10^{-9}
Onset Potential (V vs. RHE)	V_{onset}	1.587±0.001	1.587±0.001	1.623±0.001

Table S3: Constants used in modeling

Parameter	Symbol	Value	Units
Elementary Charge of Electron	q	1.602×10^{-19}	C
Boltzmann Constant	k	1.381×10^{-23}	J K^{-1}
Temperature	T	298	K
Richardson's Constant	A^*	120,000	mA cm^{-2}
Tunneling Probability Constant	$\propto$	1	Å^{-1} eV$^{-1/2}$
Doping Density	N_d	7.5×10^{15}	cm^{-3}
Si Permittivity	ε_s	11.7	unitless
Vacuum Permittivity	ε_0	8.854×10^{-14}	F cm^{-1}

Section 13 References

[1] C. A. Schneider, W. S. Rasband, K. W. Eliceiri, *Nat Methods* **2012**, *9*, 671.

[2] L. Trotochaud, S. L. Young, J. K. Ranney, S. W. Boettcher, *J. Am. Chem. Soc.* **2014**, *136*, 6744.

[3] J. Hemmerling, J. Quinn, S. Linic, *Advanced Energy Materials* **2020**, *10*, 1903354.

[4] I. A. Digdaya, B. J. Trześniewski, G. W. P. Adhyaksa, E. C. Garnett, W. A. Smith, *J. Phys. Chem. C* **2018**, *122*, 5462.

[5] L. F. Wagner, R. W. Young, A. Sugerman, *IEEE Electron Device Letters* **1983**, *4*, 320.

[6] J. R. Hemmerling, A. Mathur, S. Linic, *Acc. Chem. Res.* **2021**, *54*, 1992.

[7] E. L. Meyer, "Extraction of Saturation Current and Ideality Factor from Measuring Voc and Isc of Photovoltaic Modules," DOI 10.1155/2017/8479487can be found under https://www.hindawi.com/journals/ijp/2017/8479487/, **2017**.

[8] E. H. Rhoderick, *IEE Proceedings I - Solid-State and Electron Devices* **1982**, *129*, 1.

[9] R. T. (董梓則) Tung, *Applied Physics Reviews* **2014**, *1*, 011304.

[10] D. J. Coe, E. H. Rhoderick, *J. Phys. D: Appl. Phys.* **1976**, *9*, 965.

[11] H. C. Card, E. H. Rhoderick, *J. Phys. D: Appl. Phys.* **1971**, *4*, 1589.

[12] F. A. L. Laskowski, S. Z. Oener, M. R. Nellist, A. M. Gordon, D. C. Bain, J. L. Fehrs, S. W. Boettcher, *Nat. Mater.* **2019**, 1.

[13] G. Xu, Z. Xu, Z. Shi, L. Pei, S. Yan, Z. Gu, Z. Zou, *ChemSusChem* **2017**, *10*, 2897.

[14] G. Loget, B. Fabre, S. Fryars, C. Mériadec, S. Ababou-Girard, *ACS Energy Lett.* **2017**, *2*, 569.

[15] S. A. Lee, I. J. Park, J. W. Yang, J. Park, T. H. Lee, C. Kim, J. Moon, J. Y. Kim, H. W. Jang, *Cell Reports Physical Science* **2020**, *1*, 100219.

[16] M. T. Greiner, M. G. Helander, Z.-B. Wang, W.-M. Tang, Z.-H. Lu, *J. Phys. Chem. C* **2010**, *114*, 19777.

[17] E. L. Ratcliff, J. Meyer, K. X. Steirer, A. Garcia, J. J. Berry, D. S. Ginley, D. C. Olson, A. Kahn, N. R. Armstrong, *Chem. Mater.* **2011**, *23*, 4988.

[18] M. Javad Eslamibidgoli, A. Groß, M. Eikerling, *Physical Chemistry Chemical Physics* **2017**, *19*, 22659.

[19] S. A. Lee, T. H. Lee, C. Kim, M. G. Lee, M.-J. Choi, H. Park, S. Choi, J. Oh, H. W. Jang, *ACS Catal.* **2018**, *8*, 7261.

[20] Q. Cai, W. Hong, C. Jian, W. Liu, *Nanoscale* **2020**, *12*, 7550.

[21] Y.-H. Yeh, C.-H. Chuang, T.-Y. Yu, M.-C. Liu, Y.-J. Cheng, *International Journal of Hydrogen Energy* **2019**, *44*, 16594.

[22] M. J. Kenney, M. Gong, Y. Li, J. Z. Wu, J. Feng, M. Lanza, H. Dai, *Science* **2013**, *342*, 836.

[23] F. A. L. Laskowski, M. R. Nellist, R. Venkatkarthick, S. W. Boettcher, *Energy & Environmental Science* **2017**, *10*, 570.

[24] C.-H. Lu, G. M. T. Wong, R. Birringer, R. Dauskardt, M. D. Deal, B. M. Clemens, Y. Nishi, *Journal of Applied Physics* **2010**, *107*, 063710.

[25] R. C. Rossi, N. S. Lewis, *J. Phys. Chem. B* **2001**, *105*, 12303.